

First-principles quantum transport with electron-vibration interactions: A maximally localized Wannier functions approach

Sejoong Kim*

*Department of Physics, Massachusetts Institute of Technology, Cambridge, Massachusetts 02139, USA
and Korea Institute for Advanced Study, Seoul 130-722, Korea*

Nicola Marzari

*Theory and Simulation of Materials, École Polytechnique Fédérale de Lausanne, 1015 Lausanne, Switzerland
(Received 5 February 2013; revised manuscript received 26 April 2013; published 4 June 2013)*

We present a first-principles approach for inelastic quantum transport calculations based on maximally localized Wannier functions. Electronic-structure properties are obtained from density-functional theory in a plane-wave basis, and electron-vibration coupling strengths and vibrational properties are determined with density-functional perturbation theory. Vibration-induced inelastic transport properties are calculated with nonequilibrium Green's function techniques; since these are based on a localized orbital representation we use maximally localized Wannier functions. Our formalism is applied first to investigate inelastic transport in a benzene molecular junction connected to monoatomic carbon chains. In this benchmark system the electron-vibration self-energy is calculated either in the self-consistent Born approximation or by lowest-order perturbation theory. It is observed that upward and downward conductance steps occur, which can be understood using multieigenchannel scattering theory and symmetry conditions. In a second example, where the monoatomic carbon chain electrode is replaced with a (3,3) carbon nanotube, we focus on the nonequilibrium vibration populations driven by the conducting electrons using a semiclassical rate equation and highlight and discuss in detail the appearance of vibrational cooling as a function of bias and the importance of matching the vibrational density of states of the conductor and the leads to minimize joule heating and breakdown.

DOI: [10.1103/PhysRevB.87.245407](https://doi.org/10.1103/PhysRevB.87.245407)

PACS number(s): 71.15.-m, 72.10.-d, 73.23.-b, 73.63.-b

I. INTRODUCTION

Molecular electronic devices have been intensively studied for the past decade, having been regarded as candidates to replace silicon-based electronics. Since Aviram and Ratner proposed the concept for the first molecular rectifier in 1974,¹ a variety of molecular devices has been suggested. In addition, thanks to advancement in experimental fabrication and measurement techniques, electronic currents through molecules have been experimentally measured and investigated.²⁻⁹ Despite these efforts, there are still many issues in the practical realization of molecular electronic devices.

Understanding interactions between conducting electrons and molecular vibrations is one of the key issues to address for future applications. Vibrational excitations due to the scattering of conducting electrons can change molecular configurations and attachment geometries, affecting the functionality and performance of molecule-based devices, or in turn backscatter electrons, impeding flow. The worst-case scenario is that local heating effects might ultimately break down the junction.

Vibration-induced inelastic transport has been theoretically investigated following two directions. The first focuses on simple model Hamiltonians, e.g., a single electronic level coupled to a single phonon mode as in the Anderson-Holstein model.¹⁰⁻²⁵ Based on this simplified assumption, many novel and interesting transport properties have been predicted and investigated. However, the models used in this approach tend to be too simplified to provide detailed and accurate theoretical data that can quantitatively explain experimental results.

As an alternative, approaches based on density-functional theory (DFT) offer the chance to describe realistic systems accurately and without any adjustable parameters.^{26,27} In particular, using DFT one can routinely calculate equilibrium geometries, electronic couplings, normal modes, and electron-vibration interactions.²⁸

Transport theories can then be combined with DFT, and several approaches have been proposed.²⁹⁻⁴⁴ In particular, a nonequilibrium Green's function (NEGF) formulation, in combination with DFT, and commonly called DFT-NEGF, has been widely used in *ab initio* quantum transport problems.⁴²⁻⁴⁴ This approach is more powerful than other methods in that it can tackle not just the emergence of electron-vibration interactions, but any other type of interactions. DFT-NEGF has been successfully applied to elastic quantum transport for both zero-bias and finite-bias cases,⁴²⁻⁴⁴ and recently it has been extended to include interaction effects such as those arising from electron-vibration couplings.³⁶⁻⁴¹

DFT-NEGF requires the use of an atomic-like localized basis, since the device needs to be spatially divided into two electrodes and a molecular conductor. For this reason most DFT-NEGF calculation packages have been implemented using localized basis sets. However, a plane-wave-based calculation can provide a systematically accurate description of electronic states and, in particular, can describe in an unbiased fashion electronic states which have considerable spread in vacuum, where localized basis sets tail off. Furthermore, while basis functions used in localized-basis calculations need to be tuned depending on the types of atoms and the chemistry of the system, a plane-wave basis can describe any given system without further assumptions.

However, plane-wave calculations in periodic-boundary conditions are not suitable for the DFT-NEGF formalism. For this, maximally localized Wannier functions (MLWFs), as proposed by Marzari and Vanderbilt,^{45–47} provide the needed formulation to link delocalized and localized orbitals. Since the Wannier transformation is an exact unitary mapping, one can construct an exact, minimal set of atomic-like localized functions within an energy window of interest without losing the accuracy of plane-wave-based DFT calculations, and an MLWF approach to quantum transport has been very successfully applied to zero-bias quantum conductance calculations.^{48–52} The next step to develop an MLWF approach to quantum transport is to include interaction effects on the transport properties. In this paper we focus on extending these MLWF-based quantum transport calculations to investigate electron-vibration interaction effects on molecular junctions.

The paper is organized as follows. In Sec. II we briefly review first-principles electronic structure calculations, especially focusing on (i) density-functional perturbation theory (DFPT) to calculate vibrational properties and electron-vibrational interactions and (2) transformation of electron-vibration matrix elements from a plane-wave basis to a maximally localized Wannier function basis. In Sec. III, quantum-transport theory based on NEGFs and diagrammatic perturbation theory is summarized. We also discuss nonequilibrium vibrational populations in the presence of interactions with conducting electrons and harmonic coupling to bulk vibrations in the electrodes. In Sec. IV application results and further analysis are presented.

II. ELECTRONIC-STRUCTURE METHODS

A. Vibrational properties: Density-functional perturbation theory

In the following, the electronic structure of the device is calculated within the framework of DFT with the ground-state charge density $n(\mathbf{r})$ and Bloch wave functions $|\psi_i\rangle$ determined by solving the Kohn-Sham equations.^{26,27,54}

Vibrational properties and electron-vibration interactions are determined with DFPT,⁵⁶ with vibrational spectra and the corresponding normal modes obtained from the first-principles interatomic force constants. The key quantity needed to obtain these is the linear variation $\Delta n(\mathbf{r})$ of the charge density $n(\mathbf{r})$ with respect to ionic displacements. In DFPT,⁵⁷ $\Delta n(\mathbf{r})$ and $|\Delta\psi_i\rangle$ can be calculated self-consistently using first-order perturbation theory (see Ref. 56 for a detailed discussion on DFPT).

Electron-vibration interactions can be written in a second quantized form as follows:⁵⁸

$$\mathcal{H}_{\text{el-vib}} = \sum_{\mathbf{k}\mathbf{q}\lambda} \sum_{mn} g_{\mathbf{k}+\mathbf{q},\mathbf{k}}^{\mathbf{q}\lambda,mn} a_{\mathbf{k}+\mathbf{q}}^{\dagger m} a_{\mathbf{k}}^n (b_{-\mathbf{q}\lambda}^{\dagger} + b_{\mathbf{q}\lambda}), \quad (1)$$

where $a_{\mathbf{k}}^{\dagger n}$ ($a_{\mathbf{k}}^n$) is the electron creation (annihilation) operator for Bloch state $|\psi_{n\mathbf{k}}\rangle$. Similarly, $b_{\mathbf{q}\lambda}^{\dagger}$ ($b_{\mathbf{q}\lambda}$) is the creation (annihilation) operator for the phonon mode λ with energy $\hbar\omega_{\mathbf{q}\lambda}$ at wave vector \mathbf{q} , and $g_{\mathbf{k}+\mathbf{q},\mathbf{k}}^{\mathbf{q}\lambda,mn}$ is the electron-phonon coupling matrix element. The electron-phonon coupling matrix can be calculated from the derivative of the self-consistent Kohn-Sham potential $\Delta V_{\text{KS}}^{\mathbf{q}\lambda}$ with respect to ionic

displacements,

$$g_{\mathbf{k}+\mathbf{q},\mathbf{k}}^{\mathbf{q}\lambda,mn} = \left(\frac{\hbar}{2\omega_{\mathbf{q}\lambda}} \right)^{1/2} \langle \psi_{\mathbf{k}+\mathbf{q},m} | \Delta V_{\text{KS}}^{\mathbf{q}\lambda} | \psi_{\mathbf{k},n} \rangle, \quad (2)$$

where $\psi_{\mathbf{k},n}$ is the n th Kohn-Sham orbital wave function at wave vector \mathbf{k} , and $\Delta V_{\text{KS}}^{\mathbf{q}\lambda}$ is the response of the self-consistent Kohn-Sham potential with respect to the phonon mode λ at wave vector \mathbf{q} .⁵⁸ Following Ref. 58, $\Delta V_{\text{KS}}^{\mathbf{q}\lambda}$ is explicitly written as

$$\Delta V_{\text{KS}}^{\mathbf{q}\lambda} = \sum_{\mathbf{R}} \sum_s \frac{\partial V_{\text{KS}}}{\partial \vec{u}_{s\mathbf{R}}} \cdot \frac{\vec{v}_s^{\mathbf{q}\lambda}}{\sqrt{M_s}} \frac{e^{i\mathbf{q}\cdot\mathbf{R}}}{\sqrt{N}}, \quad (3)$$

where $\vec{u}_{s\mathbf{R}}$ is the atomic displacement for the s th basis atom at the Bravais lattice vector \mathbf{R} , $\vec{v}_s^{\mathbf{q}\lambda}$ is the phonon displacement vector of the λ th mode at wave vector \mathbf{q} , M_s is the mass of the s th basis atom, and N is the number of unit cells considered (equivalent to the number of points in the equispaced wave-function mesh sampled in reciprocal space).

B. Maximally localized Wannier functions

As discussed in Sec. I, DFT calculations based on a plane-wave basis can provide a very accurate description of the electronic structure of the system, in particular, in comparison with a localized basis set. However, since Bloch orbitals are intrinsically delocalized, they are not suitable for quantum transport calculations based on Green's functions, in which spatial separation between electrodes and the conductor is required in the Hamiltonian description. In this work MLWFs^{45–47} are used in order to transform Bloch wave functions into localized functions. Wannier functions can be calculated as

$$|\omega_{n\mathbf{R}}\rangle = \frac{1}{N_{\text{R}}} \sum_{\mathbf{k}} \sum_i \sum_{j \in N_{\text{win}}^{(\mathbf{k})}} e^{-i\mathbf{k}\cdot\mathbf{R}} |\psi_{j\mathbf{k}}\rangle U_{\text{in}}^{(\mathbf{k})} U_{ji}^{\text{dis}(\mathbf{k})}, \quad (4)$$

where $U^{\text{dis}(\mathbf{k})}$ stands for a *disentanglement* procedure in which a maximally connected subspace is extracted from the entire entangled manifold. Here, $N_{\text{win}}^{(\mathbf{k})}$ is the number of entangled bands in a desired energy window at a wave vector \mathbf{k} . The Wannier rotation matrix $U^{(\mathbf{k})}$ is determined by minimizing the mean squared spread of the resulting Wannier functions (for details on MLWFs, we refer to Refs. 45–47).

Throughout this paper, we study quasi-one-dimensional systems simulated by large supercells that contain a conducting molecule and two electrodes. For these quasi-one-dimensional systems Γ -point sampling can be safely used (if electrodes were modeled by three-dimensional bulk materials, one could use \mathbf{k} -point sampling in the plane transverse to the transport direction, with electron-vibration interactions calculated for the \mathbf{k} mesh in the plane transverse to the transport direction). For Γ -point sampling, the electronic Hamiltonian and electron-vibration interactions in the Wannier representation can be explicitly written as

$$\mathcal{H}_e = \sum_{m,n} \mathcal{H}_{mn} c_m^{\dagger} c_n, \quad (5)$$

$$\mathcal{H}_{\text{el-vib}} = \sum_{\lambda} \sum_{m,n} \mathcal{M}_{mn}^{\lambda} c_m^{\dagger} c_n (b_{\lambda}^{\dagger} + b_{\lambda}), \quad (6)$$

where

$$\mathcal{H}_{mn} = \sum_{ij} (U^{\text{dis}} U)_{im}^* \langle \psi_i | \mathcal{H}_e | \psi_j \rangle (U^{\text{dis}} U)_{jn}, \quad (7)$$

$$\mathcal{M}_{mn}^\lambda = \sqrt{\frac{\hbar}{2\omega_\lambda}} \sum_{ij} (U^{\text{dis}} U)_{im}^* \langle \psi_i | \Delta V^\lambda | \psi_j \rangle (U^{\text{dis}} U)_{jn}. \quad (8)$$

Here c_m^\dagger (c_m) is the electron creation (annihilation) operator for the Wannier state $|\omega_m\rangle$.

III. QUANTUM TRANSPORT

In order to calculate transport properties, we adopt the Meir-Wingreen formulation, which has been widely applied to mesoscopic and nanoscale transport problems based on NEGFs.⁵³ The NEGF formalism for inelastic transport can be found in Refs. 59 and 60, and it has been extensively used to study inelastic transport properties.^{14-21,36-41} In particular, it has recently been combined with first-principles methods,³⁶⁻⁴¹ and our present calculations are based on Ref. 40. Here we briefly summarize some essential elements,⁴⁰ which are useful to understand the results in the following sections.

In the Meir-Wingreen formulation,⁵³ the net electrical current I_α entering the electrode α is

$$I_\alpha = \frac{2e}{\hbar} \int_{-\infty}^{\infty} \frac{d\varepsilon}{2\pi} \text{Tr}[\Sigma_\alpha^>(\varepsilon)G^<(\varepsilon) - \Sigma_\alpha^<(\varepsilon)G^>(\varepsilon)], \quad (9)$$

where Σ_α^\lessgtr denote the lesser and greater self-energies of electrode α .⁴⁰ Full Green's functions with electron-vibration couplings are obtained by using the Dyson and Keldysh equations⁶¹⁻⁶³

$$G^{r/a} = G_0^{r/a} + G_0^{r/a} \Sigma_{\text{vib}}^{r/a} G^{r/a}, \quad (10)$$

$$G^\lessgtr = G^r (\Sigma_L^\lessgtr + \Sigma_R^\lessgtr + \Sigma_{\text{vib}}^\lessgtr) G^a. \quad (11)$$

The electron-vibration self-energies $\Sigma_{\text{vib}}^{r/a}$ and $\Sigma_{\text{vib}}^\lessgtr$ can be calculated from a diagrammatic perturbation theory.⁶¹⁻⁶³ Following Ref. 40, we use two approximations here. The first one is the self-consistent Born approximation (SCBA), in which Hartree and Fock diagrams due to electron-vibration couplings are self-consistently calculated together with Eqs. (10) and (11). The SCBA, however, is computationally very demanding. Instead, in the case of weak electron-vibration couplings, one may use lowest order perturbation theory (LOPT),^{38,40} where electron-vibration self-energies are calculated up to the second order in the electron-vibration couplings.

Due to the electron-vibration interactions, conducting electrons can exchange their energy with molecular vibrations by absorbing or emitting local vibrational quanta. Therefore the vibrational population N_λ does not in general follow a Bose-Einstein distribution.⁶⁴ In order to describe a nonequilibrium vibrational population, Ref. 40 introduced a semiclassical rate equation,

$$\frac{d}{dt} N_\lambda = \frac{P_\lambda}{\hbar\omega_\lambda} - \gamma_\lambda (N_\lambda - n_B(\hbar\omega_\lambda)), \quad (12)$$

where P_λ denotes the net power transferred to the vibrational mode λ , $\hbar\omega_\lambda$ is the vibrational energy of the λ th mode, and n_B is the Bose-Einstein distribution. The net power P_λ is also

calculated by using NEGFs:⁴⁰

$$P_\lambda = \frac{2}{\hbar} \int_{-\infty}^{\infty} \frac{d\varepsilon}{2\pi} \varepsilon \text{Tr}[\Sigma_\alpha^>(\varepsilon)G^<(\varepsilon) - \Sigma_\alpha^<(\varepsilon)G^>(\varepsilon)]. \quad (13)$$

The first term on the right-hand side of Eq. (12) represents the net molecular vibrations excited by the conducting electrons. The second term describes the heat dissipation process, which makes local vibrations equilibrated to the Bose-Einstein distribution at the temperature of the electrode. Molecular vibrations are not isolated but are mechanically coupled to the surroundings (e.g., the bulk phonons of the electrodes). Due to this coupling, local vibrations in the molecule decay into bulk phonons, and γ_λ represents this decay rate. Note that here we restrict ourselves to considering only the harmonic coupling to bulk phonons. Harmonic coupling describes *one local vibration-to-one phonon* transitions, which means that a local vibration decays by exciting one phonon mode in the electrodes.

When localized vibrations are harmonically coupled to bulk phonons (heat reservoir), the decay rate at which the λ th vibration disappears by exciting bulk phonons can be calculated by using Fermi's golden rule,⁶⁵⁻⁶⁷

$$\gamma_\lambda = \frac{2\pi}{\hbar} \sum_{k \in \text{bath}} |{}_B\langle k | \mathcal{H}_C | \lambda \rangle_S|^2 \delta(\hbar\omega_k - \hbar\omega_\lambda), \quad (14)$$

where $|\lambda\rangle_S$ and $|k\rangle_B$ denote the λ th local vibrational state and a bulk phonon state with a quantum number k , respectively, and $\hbar\omega_k$ is the phonon energy of $|k\rangle_B$. Here \mathcal{H}_C denotes the harmonic coupling between local vibrations and the heat reservoir.

In fact, Eq. (14) is equivalent to the expression

$$\gamma_\lambda = -\frac{1}{\omega_\lambda} \vec{u}_\lambda^T \text{Im} \Pi^r(\omega_\lambda) \vec{u}_\lambda, \quad (15)$$

where \vec{u}_λ is the normal mode vector of the λ th local vibration.^{68,69} $\Pi^r(\omega)$, which is defined as the retarded *heat bath self-energy*, is the mechanical counterpart to the electronic lead self-energy $\Sigma^r(\varepsilon)$.^{68,69}

Reference 39 further decomposes the first term in Eq. (12) into absorption and emission processes,

$$\frac{d}{dt} N_\lambda = (N_\lambda + 1)E_\lambda - N_\lambda A_\lambda - \gamma_\lambda (N_\lambda - n_B(\hbar\omega_\lambda)), \quad (16)$$

where A_λ and E_λ stand for absorption and emission rates.³⁹ Using Eq. (16), the steady-state solution for the vibrational populations can be immediately obtained as

$$N_\lambda = \frac{n_B(\hbar\omega_\lambda) \gamma_\lambda + E_\lambda}{A_\lambda + \gamma_\lambda - E_\lambda}. \quad (17)$$

Note that this steady-state solution exists only when $A_\lambda + \gamma_\lambda > E_\lambda$. Otherwise, Eq. (16) gives an exponentially increasing population as a function of time, indicating a vibrational instability.

IV. APPLICATIONS

In this section we present two applications of our first-principles inelastic transport approach. First, we calculate the transport properties of a benzene molecule connected to monoatomic carbon chains (cumulenes). For this benchmark

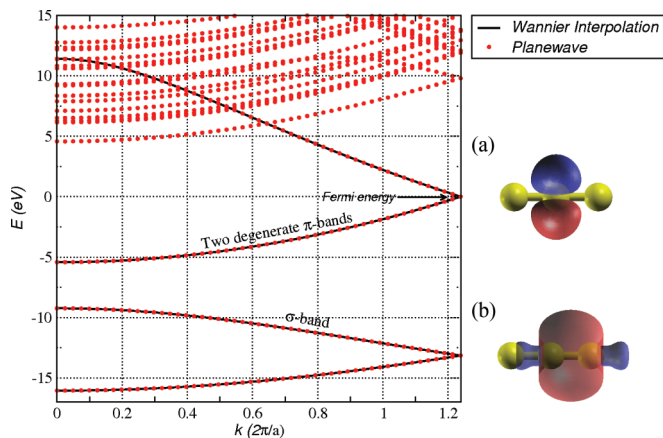


FIG. 1. (Color online) Band structure of cumulene for a two-atom unit cell. Filled (red) circles, direct DFT calculation; solid (black) lines, Wannier interpolated bands. (a) p -type Wannier function at an atomic site; (b) σ -like Wannier function at a midbond site.

system we apply both the SCBA and the LOPT for the equilibrium and nonequilibrium solutions. As the second example we replace the cumulenes with (3,3) single-wall carbon nanotubes (CNTs). In this molecular junction we focus on the calculation of realistic decay rates and nonequilibrium vibration populations. Technically, all DFT and DFPT calculations are performed using the Perdew-Zunger local-density approximation,⁷⁰ norm-conserving pseudopotentials,⁷¹ and a plane-wave basis with a cutoff of 55Ry using the QUANTUM-ESPRESSO distribution⁵⁵ and the WANNIER90 package.⁵²

A. Cumulene-benzene-cumulene junction

We first study a benzene molecule connected to a monoatomic carbon chain. It is known that cumulene is subject to a Peierls distortion: It readily becomes dimerized and opens an energy band gap favored by a lower energy structure. We thus freeze the structure of cumulene and use it as a metallic electrode. We construct two p orbitals and one σ -like midbond Wannier function (see Fig. 1) for this electrode. The two p orbitals, p_y and p_z , are perpendicular to the transport direction, which is along the x axis in our calculation. Figure 1 shows the band structure of cumulene. The energy bands are obtained either from a direct plane-wave-based DFT calculation or by Wannier band interpolation and are in excellent agreement with each other. While the lowest energy band originates from σ orbitals, p orbitals give rise to doubly degenerate π bands around the Fermi level, and transport properties at the Fermi energy are characterized by these two π bands.

Figure 2 shows the supercell geometry used in the transport calculations. The benzene molecule alone is allowed to vibrate.

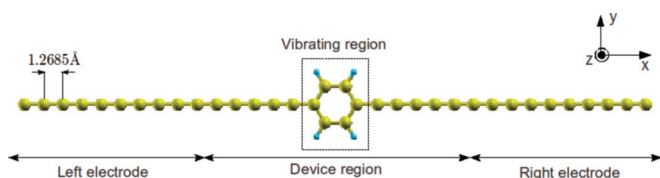


FIG. 2. (Color online) Cumulene-benzene-cumulene junction.

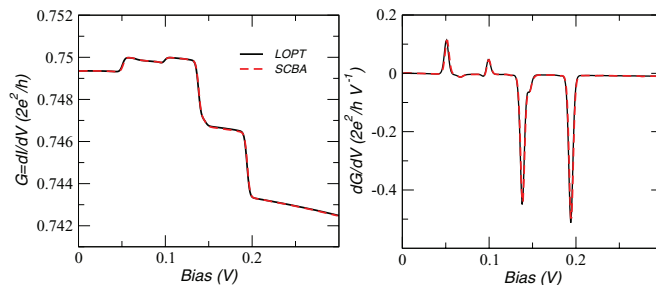


FIG. 3. (Color online) Differential conductance $G = dI/dV$ and its derivative dG/dV with equilibrium vibrational populations calculated using the LOPT [solid (black) line] or the SCBA [dashed (red) line]. At a lower bias two differential conductance increases are observed. At a higher bias, two large conductance drops occur. These conductance changes correspond to peaks in dG/dV .

The device region, containing the vibrating region and part of the cumulene, is taken to be large enough to make sure that there is no direct coupling between electrodes and that the electron-vibration coupling is 0 outside the device region. For the benzene molecule, p_z -type Wannier functions on carbon atoms and σ -like Wannier functions on C–C and C–H bonds are constructed.

The differential conductance $G = dI/dV$ and its derivative dG/dV are calculated using either the SCBA or the LOPT scheme. Temperature is taken to be $k_B T = 1\text{meV}$. As shown in Fig. 3, these two approximations display essentially perfect agreement. Four conductance changes are observed in the differential conductance curve in Fig. 3. The corresponding inelastic transport signals due to electron-vibration interactions appear as peaks in the d^2I/dV^2 plot. The peak position on the bias axis corresponds to the vibrational energy involved in the electron-vibration scattering events. From the four peaks shown in Fig. 3 one might conclude that there are four active vibrational modes, but there is a shoulder on the right side of the third peak. This may indicate that there is a fifth active vibrational mode. To investigate which vibrational modes participate in the inelastic transport, we perform *modewise* calculations by considering only one particular vibrational mode. For clarity, the elastic contribution is excluded from these modewise calculations. These calculations show that there are five major peaks in dG/dV (Fig. 4). The corresponding vibrational configurations of these five active modes are also shown: While two upward peaks are out-of-plane vibrations, three downward peaks correspond to in-plane motions. Thus, electron-vibration interactions can lead to both differential conductance rises and drops. This simultaneous occurrence can be understood from scattering theory and transmission eigenchannels,^{73,74} as discussed in Ref. 41. Let us consider an electron injected from the left electrode on a left-incident i th eigenchannel $|\Psi_L^i\rangle$ at energy ε (see Fig. 5). If there is no scattering with molecular vibrations, this electron contribution to the elastic conductance is

$$\mathcal{G}_1 = \sum_i \mathcal{T}_{L \rightarrow R}^i(\varepsilon), \quad (18)$$

where $\mathcal{T}_{L \rightarrow R}^i(\varepsilon)$ is the elastic transmission probability of $|\Psi_L^i(\varepsilon)\rangle$. Note that the conductance is normalized by the conductance quantum $G_0 = 2e^2/h$. Now let us consider that

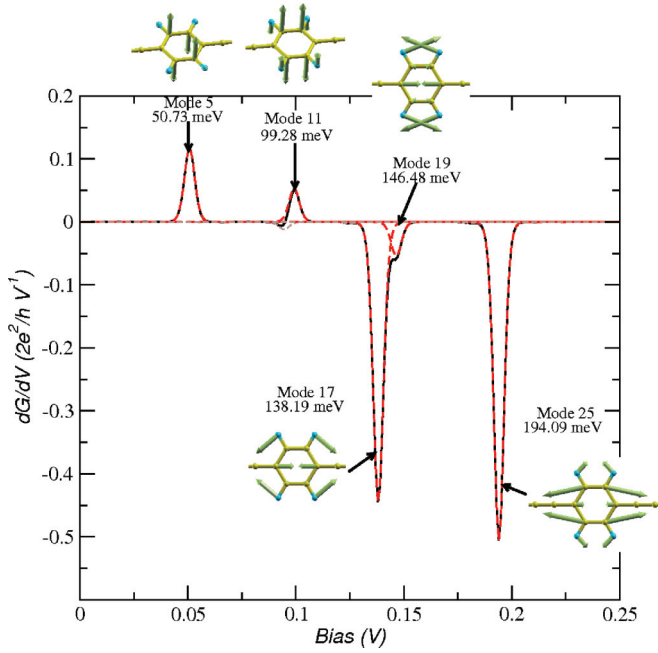


FIG. 4. (Color online) dG/dV in modewise calculation. Five active vibrational modes are found. The corresponding vibrational configurations are illustrated. While the first two active modes leading to conductance jumps are out-of-plane motions, the three conductance-drop modes correspond to in-plane vibrations.

the electron on a left-incident i th eigenchannel $|\Psi_L^i(\varepsilon)\rangle$ is scattered off to a right-incident j th eigenchannel $|\Psi_R^j(\varepsilon - \hbar\omega)\rangle$ by emitting a vibrational quantum $\hbar\omega$. The outgoing state of $|\Psi_R^j(\varepsilon - \hbar\omega)\rangle$ can go either to the left electrode or to the right one. Since conductance measured in the right lead is considered here, the probability to move back to the right electrode for $|\Psi_R^j(\varepsilon - \hbar\omega)\rangle$ is given by its reflection probability $\mathcal{R}_R^j(\varepsilon - \hbar\omega)$. If $\mathcal{P}_{i \rightarrow j}$ denotes the probability that $|\Psi_L^i(\varepsilon)\rangle$ is scattered to $|\Psi_R^j(\varepsilon - \hbar\omega)\rangle$, then the total conductance can be computed as

$$\mathcal{G}_2 = \sum_i \left(1 - \sum_j \mathcal{P}_{i \rightarrow j} \right) \mathcal{T}_{L \rightarrow R}^i(\varepsilon) + \sum_{i,j} \mathcal{P}_{i \rightarrow j} \mathcal{R}_R^j(\varepsilon - \hbar\omega). \quad (19)$$

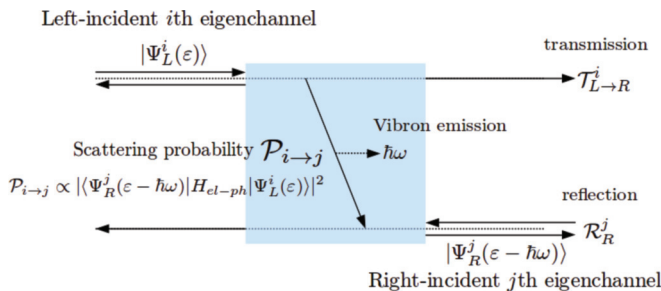


FIG. 5. (Color online) Schematic representation of inelastic scattering in the presence of electron-vibration interactions. Solid arrows indicate transmission eigenchannels.

Thus, the conductance change is given by

$$\Delta\mathcal{G} = \mathcal{G}_2 - \mathcal{G}_1 \approx \sum_{i,j} \mathcal{P}_{i \rightarrow j} (\mathcal{R}_R^j(\varepsilon_F) - \mathcal{T}_{L \rightarrow R}^i(\varepsilon_F)), \quad (20)$$

where the transmission and reflection probabilities are approximated by those at the Fermi energy ε_F (since vibrational energies are generally low, one might expect that transmission and reflection probabilities would not change significantly over $[\varepsilon_F - \hbar\omega, \varepsilon_F + \hbar\omega]$). Note that the conductance can increase or decrease depending on the relative magnitude of $\mathcal{P}_{i \rightarrow j} (\mathcal{R}_R^j(\varepsilon_F) - \mathcal{T}_{L \rightarrow R}^i(\varepsilon_F))$ and that, while $(\mathcal{R}_R^j(\varepsilon_F) - \mathcal{T}_{L \rightarrow R}^i(\varepsilon_F))$ does not depend on the vibrational configuration, $\mathcal{P}_{i \rightarrow j} \propto |\langle \Psi_R^j | \mathcal{H}_{el-vib}^\lambda | \Psi_L^i \rangle|^2$, calculated from Fermi's golden rule,^{75,76} is determined by the electron-vibration interaction matrix.

For the cumulene-benzene-cumulene system, it is found that there are two transmission eigenchannels: the major transmission channel $|\Psi_{L,R}^1\rangle$, with $\mathcal{T}_{L \rightarrow R}^1 = \mathcal{T}_{R \rightarrow L}^1 = 0.741$; and the minor channel $|\Psi_{L,R}^2\rangle$, with $\mathcal{T}_{L \rightarrow R}^2 = \mathcal{T}_{R \rightarrow L}^2 = 0.004$. p_z orbitals on the cumulene wire and the benzene molecule constitute the major transmission eigenchannel $|\Psi_{L,R}^1\rangle$. p_y orbitals on the cumulene wire and σ bonds of the benzene molecule contribute to the minor transmission channel $|\Psi_{L,R}^2\rangle$. In addition, while $|\Psi_{L,R}^1\rangle$ is symmetric with respect to the zx plane, $|\Psi_{L,R}^2\rangle$ is antisymmetric. In other words, when \hat{P}_{zx} denotes the reflection operator with respect to the zx plane, $\hat{P}_{zx}|\Psi_{L,R}^1\rangle = |\Psi_{L,R}^1\rangle$ and $\hat{P}_{zx}|\Psi_{L,R}^2\rangle = -|\Psi_{L,R}^2\rangle$ hold.

The first two active vibrational modes, $\lambda = 5$ and 11 , shown in Fig. 4 and leading to differential conductance jumps, show antisymmetric vibrational motions with respect to the zx plane. Then the corresponding electron-vibration interactions $\mathcal{H}_{el-vib}^{\lambda=5,11}$ satisfy

$$\mathcal{H}_{el-vib}^{\lambda=5,11} = -\hat{P}_{zx} \mathcal{H}_{el-vib}^{\lambda=5,11} \hat{P}_{zx}. \quad (21)$$

Because of these reflection symmetries,

$$\langle \Psi_R^1 | \mathcal{H}_{el-vib}^{\lambda=5,11} | \Psi_L^1 \rangle = \langle \Psi_R^2 | \mathcal{H}_{el-vib}^{\lambda=5,11} | \Psi_L^2 \rangle = 0, \quad (22)$$

i.e., scattering from $|\Psi_L^{1(2)}\rangle$ to $|\Psi_R^{1(2)}\rangle$ is prohibited. Since $(\mathcal{R}_R^2 - \mathcal{T}_{L \rightarrow R}^1) = (\mathcal{R}_R^1 - \mathcal{T}_{L \rightarrow R}^2) = 0.255$, one obtains a differential conductance rise:

$$\Delta\mathcal{G} = [\mathcal{P}_{1 \rightarrow 2}^{\lambda=5,11} (\mathcal{R}_R^2 - \mathcal{T}_{L \rightarrow R}^1) + \mathcal{P}_{2 \rightarrow 1}^{\lambda=5,11} (\mathcal{R}_R^1 - \mathcal{T}_{L \rightarrow R}^2)] > 0. \quad (23)$$

In contrast, the last three active modes, $\lambda = 17, 19$, and 25 , are symmetric with respect to the zx plane:

$$\mathcal{H}_{el-vib}^{\lambda=17,19,25} = \hat{P}_{zx} \mathcal{H}_{el-vib}^{\lambda=17,19,25} \hat{P}_{zx}. \quad (24)$$

Therefore, one has these reflection selection rules:

$$\langle \Psi_R^1 | \mathcal{H}_{el-vib}^{\lambda=17,19,25} | \Psi_L^2 \rangle = \langle \Psi_R^2 | \mathcal{H}_{el-vib}^{\lambda=17,19,25} | \Psi_L^1 \rangle = 0. \quad (25)$$

Since numerical calculations show that $\mathcal{P}_{1 \rightarrow 1}^{\lambda=17,19,25} \gg \mathcal{P}_{2 \rightarrow 2}^{\lambda=17,19,25}$, one finds the three differential conductance drops

$$\Delta\mathcal{G} = [\mathcal{P}_{1 \rightarrow 1}^{\lambda=17,19,25} (\mathcal{R}_R^1 - \mathcal{T}_{L \rightarrow R}^1) + \mathcal{P}_{2 \rightarrow 2}^{\lambda=17,19,25} (\mathcal{R}_R^2 - \mathcal{T}_{L \rightarrow R}^2)] < 0, \quad (26)$$

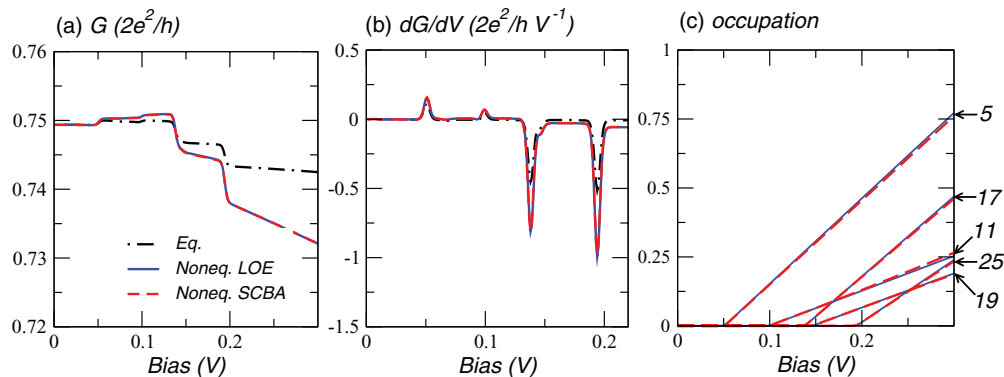


FIG. 6. (Color online) Inelastic transport calculations with nonequilibrium vibrational populations Solid (blue) line, LOPT; dashed (red) line, SCBA; dot-dashed (black) line, equilibrium case. (a) Differential conductance, (b) second derivative of the current, and (c) vibration populations.

where $(\mathcal{R}_R^1 - \mathcal{T}_{L \rightarrow R}^1) = -0.482$ and $(\mathcal{R}_R^2 - \mathcal{T}_{L \rightarrow R}^2) = 0.992$. In general, this multichannel analysis shows that differential conductance rises and drops can occur at the same time.

Next, let us take into account the effect of nonequilibrium vibrational populations on transport properties. This situation corresponds to the case where the decay rate of a molecular vibration to its surroundings is lower than the emission rate due to electron-vibration scattering. In order to compare equilibrium and nonequilibrium vibration cases the decay rate $\hbar\gamma_\lambda = 0.1\text{meV}$ has been chosen for all vibrational modes; this condition is relaxed in the next example.

As shown in Fig. 6(a), nonequilibrium effects lead to larger slopes in comparison with the equilibrium case. Furthermore, the differential conductance change increases at the threshold bias voltage. These two changes appear as (i) a finite dG/dV value between peaks and (ii) increased peak heights [see Fig. 6(b)]. When the bias exceeds the threshold voltage equal to the vibrational energy, the vibrational population starts to increase, as shown in Fig. 6(c). This is due to the increase in phase space for conducting electrons that can emit molecular vibration quanta. Recalling that electron-vibration scattering is roughly proportional to N_λ , increased vibration populations enhance inelastic transport signals in return. Finally, we also consider transport calculations where we change the decay rate and show in Fig. 7 that the differential conductance approaches the equilibrium case as the decay rate increases.

B. (3,3) CNT-benzene-(3,3) CNT

In the previous benchmark, the cumulene wire, subject to Peierls' instability, was frozen in order to maintain its metallic character, and the decay rate for molecular vibrations was used as a parameter. Here we replace the cumulene wire with a metallic (3,3) CNT, which is mechanically stable, and calculate all decay rates from the first-principles couplings.

Carbon-based nanostructures, such as CNTs and graphene, could become new platforms for future nanotechnology applications due to their excellent electronic properties. Recently, carbon-based nanojunctions have been experimentally fabricated: These include carbon chains connected to graphene⁷⁷ or CNTs⁷⁸ and organic molecules coupled to CNT electrodes with amide linkers.⁷⁹ These experimental

achievements have stimulated theoretical and computational studies on carbon-based nanodevices.^{80,81} In particular, a benzene molecule connected to CNT electrodes (which is the system of our interest) was suggested as a molecular switch, operated by controlling the relative angle between π orbitals of the benzene and the π -orbital manifold of CNT electrodes.⁸¹ Functionality and performance of molecular devices are strongly affected by molecular geometries or anchoring points to the electrodes, and they may be affected by vibrations induced by conducting electrons. In a worst-case scenario, local heating may break down the junctions.

In our work, we choose a vibrating region by defining an extended molecule in which a benzene and the outmost relaxed CNT layers are included. This extended molecule is seamlessly connected to the bulk CNT electrodes. The vibrating region contains 56 atoms in total, and these correspond to 168 vibrational modes. Figure 8 illustrates the supercell geometry used in the decay rate calculations: It contains the extended molecule and two vibrational principal layers⁷² for bulk phonons.

We proceed as follows. First, by allowing only the extended molecule to vibrate, the electron-vibration interactions $\mathcal{H}_{\text{el-vib}}$, the vibrational spectrum $\{\hbar\omega_\lambda\}$, and the corresponding normal

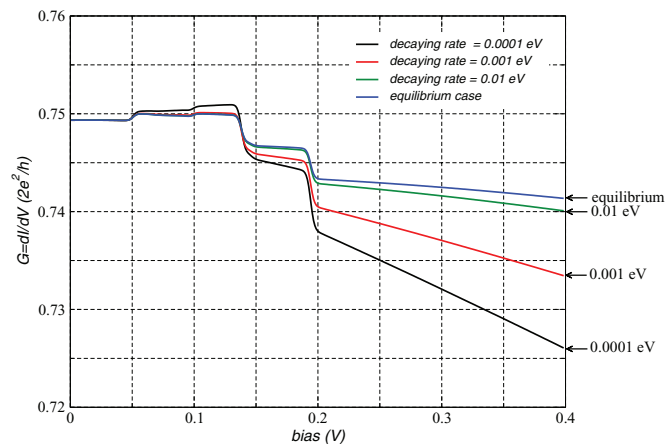


FIG. 7. (Color online) Differential conductance for different decay rates. Black line, $\hbar\gamma_\lambda = 0.1\text{meV}$; red line, $\hbar\gamma_\lambda = 1\text{meV}$; green line, $\hbar\gamma_\lambda = 10\text{meV}$; blue line, equilibrium case ($\hbar\gamma_\lambda \rightarrow \infty$).

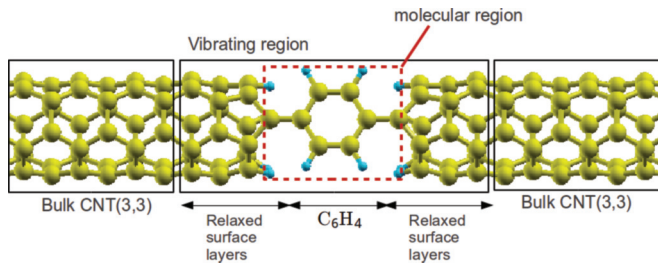


FIG. 8. (Color online) (3,3) CNT–benzene–(3,3) CNT supercell geometry used in decay rate calculations. The vibrating region contains a benzene molecule and three relaxed surface CNT layers. Dashed (red) lines represent the molecular region containing a benzene molecule, anchoring carbon atoms, and hydrogen atoms saturating the CNT edge.

modes are calculated. Then the interatomic force constants for the entire supercell in Fig. 8 are calculated. From these interatomic force constants one can extract the harmonic coupling matrix \mathcal{H}_C between the extended molecule and the bulk electrodes. In addition, we take a periodic unit cell for the bulk (3,3) CNT and calculate its interatomic force constants H_B .

The calculated decay rates are shown in Fig. 9(a), in units of electronvolts. While most of the decay rates are of the order of 10^{-2} to 10^{-3} eV, there are few modes with much lower rates. These low decay rates can arise for two reasons. First, as shown in Fig. 9(a), decay rates start to increase

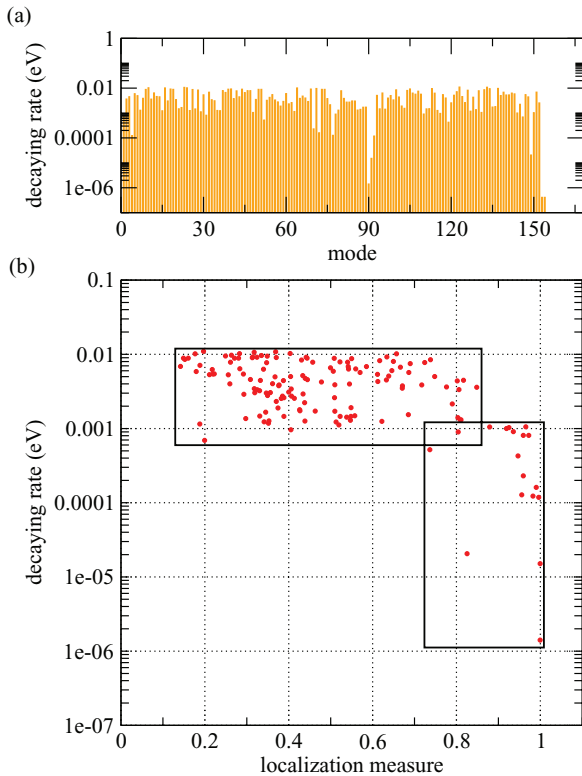


FIG. 9. (Color online) (a) Decay rates for each vibrational mode of the (3,3) CNT–benzene–(3,3) CNT junction. (b) Decay rate vs localization (see text for the definition). Decay rates are plotted on a logarithmic scale.

significantly from the 153rd mode on. These vibrational modes (between 153 and 168) have energies higher than the highest (3,3) CNT phonon energy. Recalling that decay processes based on the harmonic coupling essentially correspond to one vibration–to–one phonon transitions, there are no bulk phonons to which the vibrational modes laying outside the band width of bulk phonons can transfer their vibrational energies. Once the anharmonic coupling that makes one vibration–to–multiphonon transition possible is taken into account, these modes may have higher decay rates. However, this correction goes beyond the present approach.

Second, we can notice that even among the vibrational modes whose energies lie inside the bulk phonon dispersions, some also display low decay rates. Most of these correspond to vibrations that are localized inside the benzene molecule or to wagging motions of the surface hydrogen atoms. Because these motions are spatially well separated from bulk phonons, one may expect that they are less coupled to bulk phonons. In order to measure how localized these modes are inside the molecule, we define the benzene molecule, two anchoring carbon atoms, and the surface hydrogen atoms as the molecular region shown in Fig. 8. If \mathcal{P}_M denotes a projection operator onto a molecular region, one can find how localized the vibration is inside the molecular region from $|\mathcal{P}_M|\lambda\rangle|^2$, where $|\lambda\rangle$ indicates the vibrational state for the normal mode λ . We call $|\mathcal{P}_M|\lambda\rangle|^2$ the localization measure for vibrations. Figure 9(b) shows the relation between localization and decay rates. When the vibration is localized in the molecular region, or, equivalently, $|\mathcal{P}_M|\lambda\rangle|^2$ approaches 1, its decay rate is much lower.

Except for the modes between 153 and 168, the majority of the vibrations overlap with the phonon dispersions of the CNT electrodes. This happens due to the same chemical character between hydrocarbons and carbon-based electrodes. If we were to consider organic molecules attached to a metal electrode such as gold and platinum, the large mass difference between atoms in the molecule and those in the electrode would make most of the molecular modes lie outside the electrode phonon dispersions. Therefore, most of the vibrational modes would have very low decay rates, significantly increasing the probability of the molecular junction’s breaking down.

Using Eq. (16), we can now calculate nonequilibrium vibrational populations. Vibrational occupations will start to increase as the bias voltage exceeds their corresponding threshold voltages. While in the vicinity of the threshold voltage the vibrational populations increase linearly, nonlinear effects can appear at higher bias voltages. For low-energy modes vibrational populations monotonically increase with bias; however, nonmonotonic populations are observed for some of the high-energy modes. These trends are shown in Fig. 10, where vibrational populations N_λ and corresponding effective temperatures T_{eff}^λ for some of the highly excitable modes are illustrated. The effective temperature T_{eff}^λ is defined as $N_\lambda = \frac{1}{e^{\hbar\omega_\lambda/k_B T_{\text{eff}}^\lambda} - 1}$. Mode 1, which is low energy, shows a monotonically increasing behavior. For the other high-energy modes, their populations increase, then decrease in a certain bias voltage range and then start to increase again, giving rise effectively to the phenomenon of *vibrational cooling*⁸² (Fig. 10).

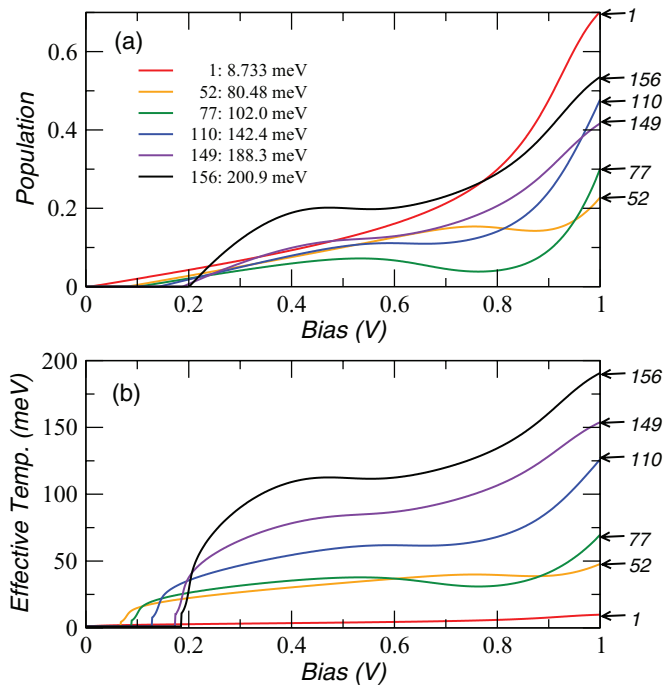


FIG. 10. (Color online) (a) Nonequilibrium vibrational populations and (b) effective temperature T_{eff}^{λ} for the most excitable modes as a function of the bias voltage. Vibrational configurations of the modes are shown in Fig. 11.

One can hint at a qualitative explanation for this cooling behavior by examining the local density of states in the device region, as recently discussed in Ref. 82. As shown in Fig. 12(a), there is one resonant peak located at an energy higher than μ_{eq} , which is the common Fermi level before a bias is applied. Figure 12(b) shows absorption and emission processes where electrons can exploit the resonant density of states for different bias voltages. Red and blue lines indicate

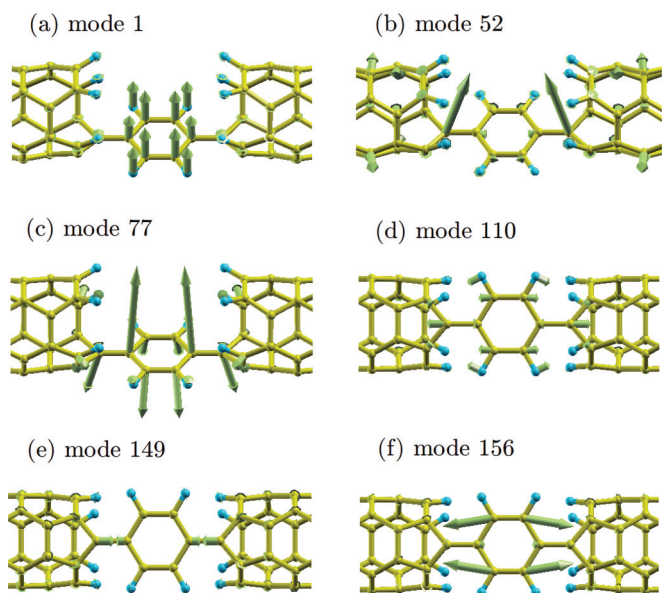


FIG. 11. (Color online) Vibrational configurations for the modes discussed in Fig. 10.

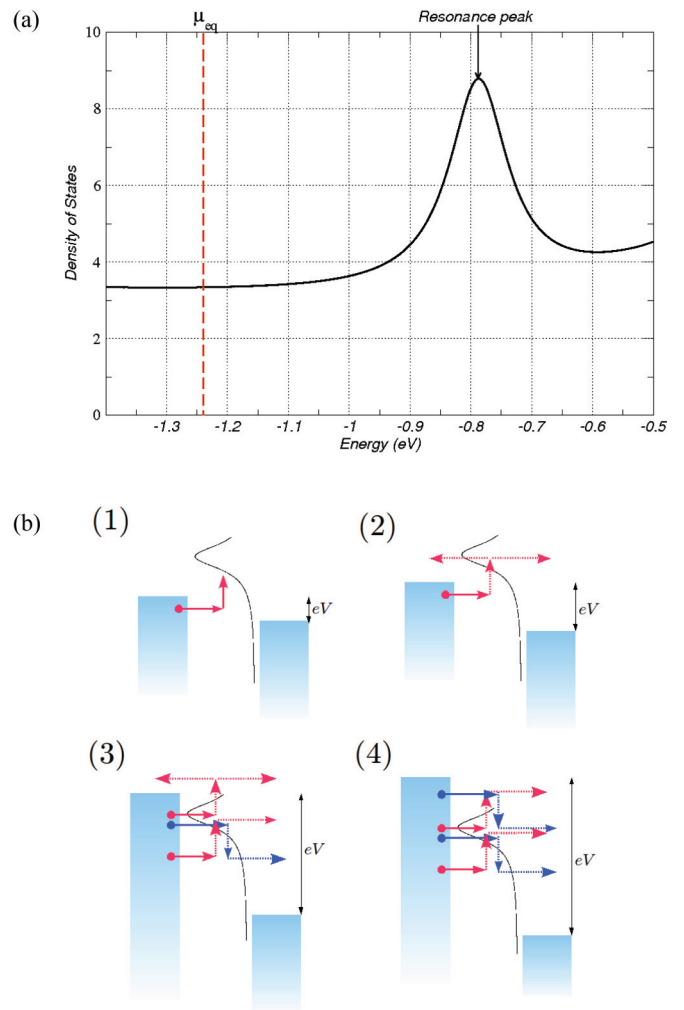


FIG. 12. (Color online) (a) density of states for the device region. Close to the equilibrium Fermi level, one resonance peak is found. (b) absorption (red arrow line) and emission (blue arrow line) processes taking place via the resonant peak as the bias voltage increases.

absorption and emission processes, respectively. For a very small bias none of the electrons can access the resonant peak, as shown in Fig. 12(b), 1. When the bias increases, the absorption process using the resonant peak starts to take place, but the electrons participating in the emission process cannot reach the resonance [see Fig. 12(b), 2]. Therefore, the absorption rate A_{λ} becomes enhanced, so it may lead to a decrease in vibrational populations. For higher biases such that the resonant peak is located between the left and the right chemical potentials, the emission process using resonance is activated, leading to enhanced emission rates, as shown in Fig. 12(b), 3. When the bias increases even more, another resonant emission process becomes possible, as shown in Fig. 12(b), 4, while the resonant absorption process at which the electrons are reflected back to the left lead is prohibited due to Pauli blocking. As a result, the emission rate is enhanced more in comparison to the absorption one, and vibrational populations may increase again in this bias range. As an illustrative example, Fig. 13(b) shows the absorption and emission rates for mode 156. One can clearly observe that the bias voltages for which the absorption and emission rates get enhanced are different: The slope of the

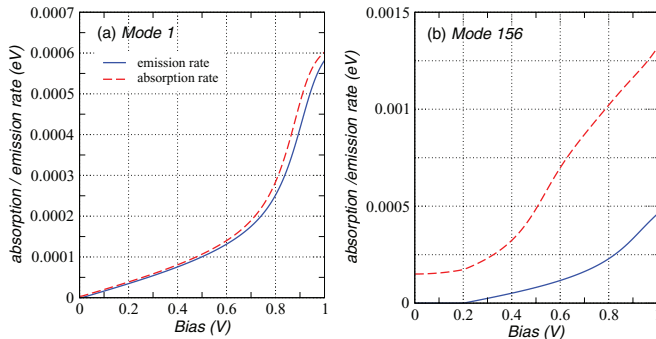


FIG. 13. (Color online) Absorption (red dashed line) and emission (blue solid line) rates for (a) vibrational mode 1 (low-energy mode) and (b) 156 (high-energy mode)

absorption rate curve first increases around 0.4V but then decreases at 0.7V. By contrast, the emission rate linearly increases up to 0.8V, and at a bias larger than 0.8V its slope also increases. The difference in bias voltages at which absorption and emission rates become enhanced results in the cooling behavior observed in the intermediate bias range.

For low-energy modes whose energies are much lower than the broadening of the resonant peak, the intermediate cooling regime may not appear distinctly. For example, see in Fig. 13(a) the absorption and emission rates for mode 1. Unlike mode 156, the absorption and emission rates show quite similar dependences on the bias voltage, implying that a cooling behavior is not observed.

Finally, not every high-energy mode will necessarily go through a cooling phase, since vibrational populations are determined by the interplay of absorption, emission, and decay rates. When the decay rate γ_λ is higher than the difference between the absorption and the emission rates $A_\lambda - E_\lambda$, the steady-state solution can be approximated as

$$N_\lambda = \frac{n_B(\hbar\omega_\lambda)\gamma_\lambda + E_\lambda}{\gamma_\lambda + A_\lambda - E_\lambda} \approx n_B(\hbar\omega_\lambda) + \frac{E_\lambda}{\gamma_\lambda}. \quad (27)$$

In this case, the dependence of the vibrational population on the bias voltage becomes similar to that of the emission rate, and a cooling behavior does not appear.

Finally, we would like to stress the importance of mass ratios between the conducting molecule and electrodes. As pointed out above, since the band width of bulk phonons in the electrodes gets smaller as the atomic mass of the electrodes increases, a molecular junction connected to electrodes consisting of heavier atoms will have fewer opportunities to thermalize. To demonstrate this mass ratio effect, we calculate the total vibrational energy stored in the vibrating region by increasing the mass of the atoms in the carbon electrode, to model, e.g., silicon or germanium. As shown in Fig. 14, the junction with a higher mass ratio has more vibrational energy, and a higher probability of breaking down due to heating effects.

Before concluding, we note that in this work, electronic structure properties have been calculated at equilibrium, while the finite-bias effect is considered only in the transport calculations based on the NEGF formalism. This approach is valid in a low bias regime. In contrast, in a high bias regime, the finite bias could affect the electronic-structure properties

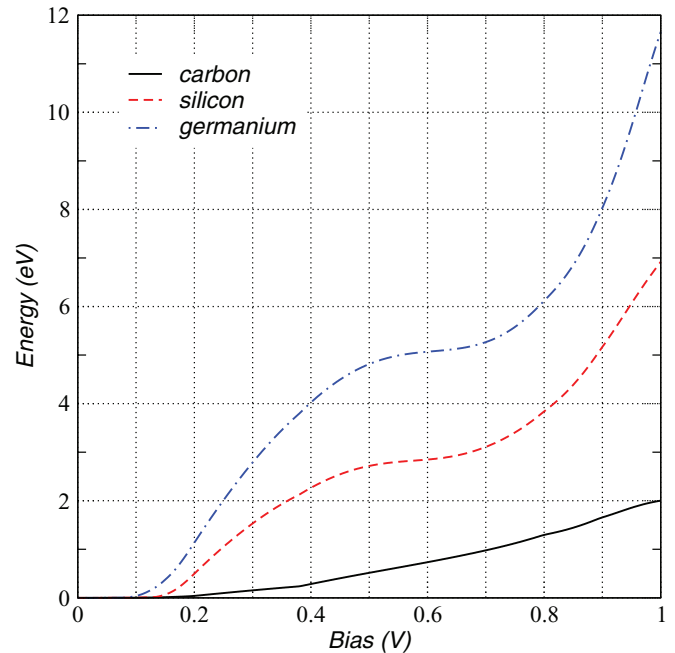


FIG. 14. (Color online) Total vibrational energy stored in the vibrating region, as a function of the mass of the electrode atom. Solid (black) line, carbon; dashed (red) line, silicon; dot-dashed (blue) line, germanium.

such as charge densities, electron-vibration interactions, and vibrational frequencies. In fact, Ref. 83 investigated the finite-bias effect on the electron-vibration coupling strengths and vibrational spectrum, showing that the electron-vibration coupling strengths can be drastically enhanced (for the system studied) above 0.5 V.

V. SUMMARY

In this work we have described a first-principles quantum approach based on MLWFs to calculate inelastic transport properties in the presence of electron-vibration interactions. In our implementation, calculations are performed using the plane-wave DFT and DFPT QUANTUM-ESPRESSO distribution⁵⁵ and transformation into a MLWF representation and the construction of Hamiltonians in the Wannier basis using WANNIER90.⁵² Inelastic transport properties such as differential conductance and nonequilibrium vibrational occupations have been calculated within the Meir-Wingreen transport formalism based on the NEGF. In particular, the electron-vibration self-energy is computed using either the SCBA or the LOPT. We have tested our implementation by applying it to carbon-based molecular junctions: a benzene molecule connected to cumulene chains and a (3,3) CNT-benzene-(3,3) CNT junction.

In the first system we have found differential conductance changes at bias voltages corresponding to the vibrational energies of active modes. Using a multieigenchannel analysis based on scattering theory, we have identified that out-of-plane and in-plane vibrational motions lead to conductance jumps and drops, respectively. This analysis of the simultaneous occurrence of conductance jumps and drops is consistent with recently reported calculations.⁴¹

In the second application, where cumulene wires are replaced with realistic CNT electrodes, we have focused on the decay rates of molecular vibrations and nonequilibrium vibrational populations. Low decay rates can be rationalized by examining the band width of bulk phonons that molecular vibration can resonantly access and the localization of molecular vibrations. Also, we have argued that a higher mass ratio between the conducting molecule and electrodes can enhance local heating and ultimately lead to junction breakdown. Thus, organic molecular junctions connected to carbon-based electrodes or lighter metals may be more stable in comparison to heavy-metal electrodes (of course, the strength of the anchoring chemical bonds will also play a role). We have also observed that nonequilibrium vibrational occupations for high-energy modes can be cooled down in an intermediate bias

regime, which may be understood in terms of a resonant state in the device region. This observation agrees well with resonant cooling reported in other first-principle calculations.⁸²

These applications and detailed analysis, in very good agreement with other first-principle studies, confirm that our first-principles approach to inelastic transport with plane-wave basis and Wannier functions can be applied in all generality to other realistic nanoscale junctions.

ACKNOWLEDGMENTS

We are especially grateful to J. D. Joannopoulos for many helpful discussions and to N. Bonini, D. Ceresoli, C.-H. Park, and X. Qian. S. Kim acknowledges financial support from the Samsung Scholarship.

*sejoong@kias.re.kr

- ¹A. Aviram and M. A. Ratner, *Chem. Phys. Lett.* **29**, 277 (1974).
- ²M. A. Reed, C. Zhou, C. J. Muller, T. P. Burgin, and J. M. Tour, *Science* **278**, 252 (1997).
- ³B. C. Stipe, M. A. Rezael, and W. Ho, *Science* **280**, 1732 (1998).
- ⁴R. H. M. Smit, Y. Noat, C. Untiedt, N. D. Lang, M. C. van Hemert, and J. M. van Ruitenbeek, *Nature (London)* **419**, 906 (2002).
- ⁵L. Venkataraman, J. E. Klare, C. Nuckolls, M. S. Hybertsen, and M. L. Steigerwald, *Nature* **442**, 904 (2006).
- ⁶E. Scheer, N. Agrat, J. C. Cuevas, A. Levy Yeyati, B. Ludoph, A. Martn-Rodero, G. Rubio Bollinger, J. M. van Ruitenbeek and C. Urbina, *Nature* **394**, 154 (1998).
- ⁷A. I. Yanson, G. Rubio Bollinger, H. E. van den Brom, N. Agrat, and J. M. van Ruitenbeek, *Nature* **395**, 783 (1998).
- ⁸N. Agraït, C. Untiedt, G. Rubio-Bollinger, and S. Vieira, *Phys. Rev. Lett.* **88**, 216803 (2002).
- ⁹B. Q. Xu and N. J. J. Tao, *Science* **301**, 1221 (2003).
- ¹⁰J. Koch and F. von Oppen, *Phys. Rev. Lett.* **94**, 206804 (2005).
- ¹¹J. Koch, M. E. Raikh, and F. von Oppen, *Phys. Rev. Lett.* **96**, 056803 (2006).
- ¹²J. Koch, F. von Oppen, and A. V. Andreev, *Phys. Rev. B* **74**, 205438 (2006), and references therein.
- ¹³P. S. Cornaglia, H. Ness, and D. R. Grempel, *Phys. Rev. Lett.* **93**, 147201 (2004).
- ¹⁴M. Galperin, A. Nitzan, and M. A. Ratner, *Phys. Rev. B* **73**, 045314 (2006).
- ¹⁵M. Galperin, A. Nitzan, and M. A. Ratner, *Phys. Rev. B* **74**, 075326 (2006).
- ¹⁶M. Galperin, A. Nitzan, and M. A. Ratner, *Phys. Rev. B* **75**, 155312 (2007).
- ¹⁷M. Galperin, A. Nitzan, and M. A. Ratner, *Phys. Rev. B* **76**, 035301 (2007).
- ¹⁸M. Galperin, A. Nitzan, and M. A. Ratner, *Phys. Rev. B* **78**, 125320 (2008), and references therein.
- ¹⁹D. A. Ryndyk and J. Keller, *Phys. Rev. B* **71**, 073305 (2005).
- ²⁰D. A. Ryndyk, M. Hartung, and G. Cuniberti, *Phys. Rev. B* **73**, 045420 (2006).
- ²¹D. A. Ryndyk and G. Cuniberti, *Phys. Rev. B* **76**, 155430 (2007).
- ²²D. A. Ryndyk, P. D'Amico, G. Cuniberti, and K. Richter, *Phys. Rev. B* **78**, 085409 (2008).

- ²³K. Flensberg, *Phys. Rev. B* **68**, 205323 (2003).
- ²⁴S. Braig and K. Flensberg, *Phys. Rev. B* **68**, 205324 (2003).
- ²⁵J. Paaske and K. Flensberg, *Phys. Rev. Lett.* **94**, 176801 (2005), and references therein.
- ²⁶P. Hohenberg and W. Kohn, *Phys. Rev.* **136**, B864 (1964).
- ²⁷W. Kohn and L. J. Sham, *Phys. Rev.* **140**, A1133 (1965).
- ²⁸N. Mounet and N. Marzari, *Phys. Rev. B* **71**, 205214 (2005).
- ²⁹N. Lorente and M. Persson, *Phys. Rev. Lett.* **85**, 2997 (2000).
- ³⁰N. Lorente, M. Persson, L. J. Lauhon, and W. Ho, *Phys. Rev. Lett.* **86**, 2593 (2001).
- ³¹Y. C. Chen, M. Zwolack, and M. Di Ventra, *Nano Lett.* **3**, 1691 (2003).
- ³²Y. C. Chen, M. Zwolack, and M. Di Ventra, *Nano Lett.* **4**, 1709 (2004).
- ³³Y. C. Chen, M. Zwolack, and M. Di Ventra, *Nano Lett.* **5**, 621 (2005).
- ³⁴J. Jiang, M. Kula, W. Lu, and Y. Luo, *Nano Lett.* **5**, 1551 (2005).
- ³⁵A. Troisi and M. A. Ratner, *Phys. Rev. B* **72**, 033408 (2005).
- ³⁶A. Pecchia, A. Gagliardi, S. Sanna, T. Frauenheim, and A. Di Carlo, *Nano Lett.* **4**, 2109 (2004).
- ³⁷T. Frederiksen, M. Brandbyge, N. Lorente, and A.-P. Jauho, *Phys. Rev. Lett.* **93**, 256601 (2004).
- ³⁸M. Paulsson, T. Frederiksen, and M. Brandbyge, *Phys. Rev. B* **72**, 201101 (2005).
- ³⁹A. Pecchia, G. Romano, and A. Di Carlo, *Phys. Rev. B* **75**, 035401 (2007).
- ⁴⁰T. Frederiksen, M. Paulsson, M. Brandbyge, and A.-P. Jauho, *Phys. Rev. B* **75**, 205413 (2007), and references therein.
- ⁴¹I. S. Kristensen, M. Paulsson, K. S. Thygesen, and K. W. Jacobsen, *Phys. Rev. B* **79**, 235411 (2009).
- ⁴²J. Taylor, H. Guo, and J. Wang, *Phys. Rev. B* **63**, 245407 (2001).
- ⁴³M. Brandbyge, J. L. Mozos, P. Ordejón, J. Taylor, and K. Stokbro, *Phys. Rev. B* **65**, 165401 (2002).
- ⁴⁴J. J. Palacios, A. J. Pérez-Jiménez, E. Louis, E. San Fabián, and J. A. Vergés, *Phys. Rev. B* **66**, 035322 (2002).
- ⁴⁵N. Marzari and D. Vanderbilt, *Phys. Rev. B* **56**, 12847 (1997).
- ⁴⁶I. Souza, N. Marzari, and D. Vanderbilt, *Phys. Rev. B* **65**, 035109 (2001).
- ⁴⁷N. Marzari, A. A. Mostofi, J. R. Yates, I. Souza, and D. Vanderbilt, *Rev. Mod. Phys.* **84**, 1419 (2012).

- ⁴⁸Y.-S. Lee, M. Buongiorno Nardelli, and N. Marzari, *Phys. Rev. Lett.* **95**, 076804 (2005).
- ⁴⁹Y.-S. Lee and N. Marzari, *Phys. Rev. Lett.* **97**, 116801 (2006).
- ⁵⁰E. Y. Li, N. Poilvert, and N. Marzari, *ACS Nano* **5**, 4455 (2011).
- ⁵¹M. Shelley, N. Poilvert, A. A. Mostofi, and N. Marzari, *Comput. Phys. Commun.* **182**, 2174 (2011).
- ⁵²A. A. Mostofi, J. R. Yates, Y.-S. Lee, I. Souza, D. Vanderbilt, and N. Marzari, *Comput. Phys. Commun.* **178**, 685 (2008).
- ⁵³Y. Meir and N. S. Wingreen, *Phys. Rev. Lett.* **68**, 2512 (1992).
- ⁵⁴R. Martin, *Electronic Structure: Basic Theory and Practical Methods* (Cambridge University Press, Cambridge, 2004).
- ⁵⁵P. Giannozzi *et al.*, *J. Phys.: Condens. Matter* **21**, 395502 (2009).
- ⁵⁶S. Baroni, S. de Gironcoli, A. Dal Corso, and P. Giannozzi, *Rev. Mod. Phys.* **73**, 515 (2001).
- ⁵⁷S. Baroni, P. Giannozzi, and A. Testa, *Phys. Rev. Lett.* **59**, 2662 (1987).
- ⁵⁸M. Wierzbowska, S. de Gironcoli, and P. Giannozzi, [arXiv:cond-mat/0504077](https://arxiv.org/abs/cond-mat/0504077).
- ⁵⁹C. Caroli, D. Saint-James, R. Combescot, and P. Nozieres, *J. Phys. C* **5**, 21 (1972).
- ⁶⁰P. Hyldgaard, S. Hershfield, J. H. Davies, and J. W. Wilkins, *Ann. Phys.* **236**, 1 (1994).
- ⁶¹J. Rammer and H. Smith, *Rev. Mod. Phys.* **58**, 323 (1986).
- ⁶²J. Rammer, *Quantum Field Theory of Non-equilibrium States* (Cambridge University Press, Cambridge, 2011).
- ⁶³H. Haug and A.-P. Jauho, *Quantum Kinetics in Transport and Optics of Semiconductors* (Springer, Berlin, 2010).
- ⁶⁴D. R. Ward, D. A. Corley, J. M. Tour, and D. Natelson, *Nature Nanotech.* **6**, 33 (2011).
- ⁶⁵I. Andrianov and P. Saalfrank, *J. Chem. Phys.* **124**, 034710 (2006).
- ⁶⁶S. Sakong, P. Kratzer, X. Han, K. Laß, O. Weingart, and E. Hasselbrink, *J. Chem. Phys.* **129**, 174702 (2008).
- ⁶⁷S. Sakong and P. Kratzer, *J. Chem. Phys.* **133**, 054505 (2010).
- ⁶⁸G. Romano, A. Pecchia, and A. Di Carlo, *J. Phys.: Condens. Matter* **19**, 215207 (2007).
- ⁶⁹M. Engelund, M. Brandbyge, and A. P. Jauho, *Phys. Rev. B* **80**, 045427 (2009).
- ⁷⁰J. P. Perdew and A. Zunger, *Phys. Rev. B* **23**, 5048 (1981).
- ⁷¹N. Troullier and J. L. Martins, *Phys. Rev. B* **43**, 1993 (1991).
- ⁷²D. H. Lee and J. D. Joannopoulos, *Phys. Rev. B* **23**, 4988 (1981).
- ⁷³M. Brandbyge, M. R. Sorensen, and K. W. Jacobsen, *Phys. Rev. B* **56**, 14956 (1997).
- ⁷⁴M. Paulsson and M. Brandbyge, *Phys. Rev. B* **76**, 115117 (2007).
- ⁷⁵M. J. Montgomery, J. Hoekstra, T. N. Todorov, and A. P. Sutton, *J. Phys.: Condens. Matter* **15**, 731 (2003).
- ⁷⁶M. J. Montgomery and T. N. Todorov, *J. Phys.: Condens. Matter* **15**, 8781 (2003).
- ⁷⁷C. Jin, H. Lan, L. Peng, K. Suenaga, and S. Iijima, *Phys. Rev. Lett.* **102**, 205501 (2009).
- ⁷⁸F. Börrnert, C. Börrnert, S. Gorantla, X. Liu, A. Bachmatiuk, J.-O. Joswig, F. R. Wagner, F. Schäffel, J. H. Warner, R. Schönfelder, B. Rellinghaus, T. Gemming, J. Thomas, M. Knupfer, B. Büchner, and M. H. Rummeli, *Phys. Rev. B* **81**, 085439 (2010).
- ⁷⁹X. Guo, J. P. Small, J. E. Klare, Y. Wang, M. S. Purewal, I. W. Tam, B. H. Hong, R. Caldwell, L. Huang, S. O'brien, J. Yan, R. Breslow, S. J. Wind, J. Hone, P. Kim, and C. Nuckolls, *Science* **311**, 356 (2006).
- ⁸⁰S.-H. Ke, H. U. Baranger, and W. Yang, *Phys. Rev. Lett.* **99**, 146802 (2007).
- ⁸¹T. B. Martins, A. Fazzio, and A. J. R. da Silva, *Phys. Rev. B* **79**, 115413 (2009).
- ⁸²G. Romano, A. Gagliardi, A. Pecchia, and A. Di Carlo, *Phys. Rev. B* **81**, 115438 (2010).
- ⁸³N. Sergueev, D. Roubtsov, and H. Guo, *Phys. Rev. Lett.* **95**, 146803 (2005).